

Aerodynamics of 2D and 3D Flapping Wings in Water Treading Motion

Y.J. Lee¹, K.B. Lua¹, H. Lu¹, S.N. Aisyah¹ and T.T. Lim¹

¹Department of Mechanical Engineering
 National University of Singapore, Singapore 117575, Republic of Singapore

Abstract

Flying insects demonstrate extraordinary flight performance and have inspired the design of flapping wing micro air vehicles (FWMAVs). However, FWMAVs are not confined to undergoing the same wing kinematics as those observed on natural flyers. Rather than undergoing the ubiquitous normal hovering motion typically observed on flying insects, FWMAVs may instead opt to undergo the water treading motion which originates from aquatic propulsion. In this study, the aerodynamic performance of normal hovering and water treading motions are compared for 2D and 3D rigid flapping wings in hover. Numerical simulations are conducted at varying mid-stroke angles of attack (α_M). The results show that for both 2D and 3D, water treading can achieve higher maximum mean lift coefficient compared to normal hovering. Additionally, water treading is more efficient than normal hovering at any target mean lift coefficient within the parameter range considered. Visualisation of the flow structures indicate that the performance augmentation of water treading motion can be attributed to three mechanisms. Firstly, compared to normal hovering, water treading motion delays the shedding of the leading-edge vortex. Secondly, water treading tends to yield more beneficial wing-wake interaction. Thirdly, normal hovering enters a high angle of attack (α), high drag phase near stroke reversal, which incurs high aerodynamic power. This high α phase is absent in water treading, resulting in higher efficiency. For 3D cases, the leading-edge vortex is more stable and hence the first and the second mechanisms become less significant. At $\alpha_M=45^\circ$, water treading outperforms normal hovering in terms of hovering efficiency by up to 54% in 2D and 29% in 3D. Hence, the water treading motion is a promising alternative for FWMAV.

Introduction

The flapping wing micro air vehicle concept (FWMAV) has gained much research attention recently due to advantages such as the ability to hover and to operate more efficiently at low Reynolds number (Re) compared to fixed [12] and rotary [17] wing vehicles. The performance of insect-like flapping wings can be attributed to the highly three-dimensional (3D) and unsteady flow field generated by the wings' reciprocating motions, which give rise to aerodynamic mechanisms such as a stable leading-edge vortex (LEV) [8], rotational lift [1], wing-wake interaction and the clap-and-fling mechanism [8, 16]. Developments in flapping wing aerodynamics have been summarised in several comprehensive reviews [2, 9, 11, 13].

The motion of insect wings in hover can be divided into two main categories, namely, normal hovering (NH) and dragonfly hovering (DH) motions [15]. NH is a common motion profile that features symmetric strokes along a horizontal stroke plane while DH features asymmetric strokes along an inclined stroke plane [15]. For both NH and DH, the wing begins each stroke at a high angle of attack (α) and pitches down as the wing accelerates. Near the end of the stroke, the wing pitches up as it decelerates. A schematic drawing of NH is shown in figure 1a.

The water treading motion (WT) is an alternative wing motion which originated from aquatic propulsion [14] (i.e. sculling). Unlike NH and DH, WT begins each stroke with the wing almost parallel to the stroke plane and pitches up as the wing accelerates. Near the end of the stroke, the wing pitches down as it decelerates. This is shown schematically in figure 1b. WT was first investigated by [3, 14] for two-dimensional (2D) airfoils and past simulations have shown that WT can generate higher lift and lower drag compared to NH [14]. This brings to question whether it is advantageous for a FWMAV to undergo WT instead of the more conventional NH. Hence, in this numerical study, we subject 2D and 3D wings to NH and WT and compare their aerodynamic performance in terms of lift generation and hovering efficiency.

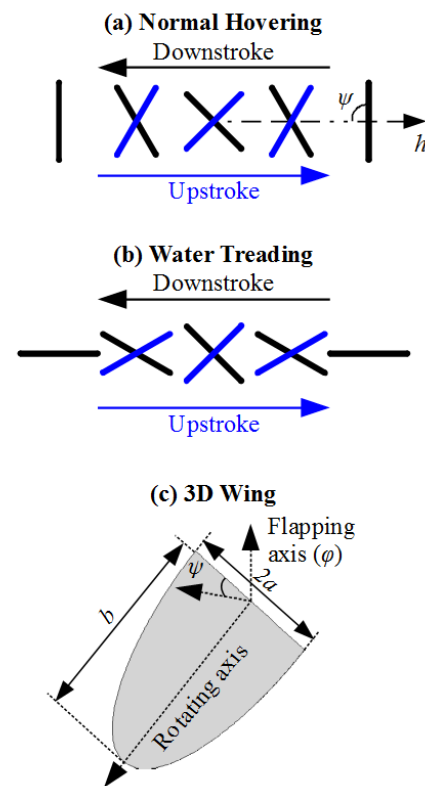


Figure 1. Schematic drawing of (a) normal hovering and (b) water treading motions. The black plates show the downstroke while the blue plates show the upstroke. (c) shows the geometry of the semi-elliptical 3D wing and the axes of flapping and rotating motions.

Methodology

Wing Geometry

This study compares the aerodynamic performance of 2D and 3D wings undergoing NH and WT. In 2D, the wing consists of a flat plate with thickness equivalent to 2% chord (c). In 3D, the wing consists of a flat plate with a semi-elliptical planform (see figure 1c), where $b/a=4.71$. Based on the semi-elliptical planform, the

planform area, $S=\pi ab/2$ and mean chord, $c=S/b=\pi a/2$. This yields aspect ratio, $AR=b/c=3$.

Wing Kinematics

In 2D, the wing kinematics are separated into the heaving motion (h) and the rotating (or pitching) motion (ψ) as shown in figure 1a. In 3D, the kinematics are separated into the flapping motion (φ) and the rotating motion (ψ) as shown in figure 1c. The 2D heaving and 3D flapping motions are defined in equations (1) and (2), respectively, where t^* is the time normalised by the duration of one flapping cycle. Both 2D and 3D motions begin with the downstroke, and the rotating motions for NH and WT are defined in equations (3) and (4), respectively, where α_M is the mid-stroke α . Based on equations (1) to (4), $\alpha=\psi$ during downstrokes and $\alpha=(180^\circ-\psi)$ during upstrokes.

$$h = h_0 \cos(2\pi t^*) \quad (1)$$

$$\varphi = \varphi_0 \cos(2\pi t^*) \quad (2)$$

$$\psi_{NH} = 90^\circ - (90^\circ - \alpha_M) \sin(2\pi t^*) \quad (3)$$

$$\psi_{WT} = \alpha_M \sin(2\pi t^*) \quad (4)$$

The reference velocities are defined as $U_{ref}=4hof$ and $U_{ref}=4(\varphi_0 R_2)f$ for the 2D and 3D cases, respectively, and R_2 is radius of gyration of the wing [6]. Here, $R_2=1.5c$. In the present non-dimensional framework, c and f are assumed to be unity, $h_0=1.5$ and $\varphi_0=1.0$ rad. This yields $U_{ref}=6$ for both 2D and 3D cases. Accordingly, kinematic viscosity (ν) is set to 0.006, yielding $Re=cU_{ref}/\nu=1,000$. Numerical simulations are conducted from $\alpha_M=25^\circ$ to 75° at intervals of 10° .

Computational Fluid Dynamics

Numerical simulations are conducted using the commercial software ANSYS® FLUENT, Release 15. The flow is assumed to be transient and turbulent; the standard $k-\varepsilon$ turbulence model is applied. Spatial and temporal discretisation schemes are second order accurate. Wing kinematics are imposed using the sliding mesh feature of the solver which imposes a rigid computational grid. The boundary conditions consist of a non-slip wall that represents the wing and a zero gauge pressure outer boundary. Based on grid and domain size convergence study, the 2D mesh has a circular computational domain of $16c$ radius and consists of 20 thousand elements. The 3D mesh has a spherical computational domain of $10c$ radius and consists of 0.9 million elements. Lift coefficient (C_L) and power coefficient (C_P) are computed based on equations (5) and (6), where ρ , F_L and P refer to fluid density, lift force and aerodynamic power, respectively.

$$C_L = F_L / (0.5 \rho S U_{ref}^2) \quad (5)$$

$$C_P = P / (0.5 \rho S U_{ref}^3) \quad (6)$$

The 2D simulations are validated by simulating the ‘‘no ground’’, $\alpha_M=45^\circ$ experiment from [5] and the 3D simulations are validated by simulating the honey bee experiment from [4]. Figure 2 compares the C_L of present CFD against past experimental measurements from [4, 5] and the agreement is reasonable.

Results

In the simulations, periodic state is achieved after the first four flapping cycles. Accordingly, C_L and C_P are obtained from the fifth flapping cycle ($t^*=4$ to 5) and time-averaged to yield $C_{L,avg}$ and $C_{P,avg}$. Similar to the previous works in [7, 10], hovering efficiency is represented here by the ratio of $C_{L,avg}/C_{P,avg}$. Figure 3 shows the

plot of $C_{L,avg}/C_{P,avg}$ against $C_{L,avg}$. It is apparent from figure 3 that in 2D, WT results in significant higher aerodynamic performance compared to NH. Specifically, WT is able to achieve significantly higher $C_{L,avg}$ and is significantly more efficient than NH when both motions are generating similar values of $C_{L,avg}$. In 3D, the enhancement in aerodynamic performance offered by WT is modest. Nevertheless, WT does generate higher value of maximum $C_{L,avg}$ and achieves slightly improved hovering efficiency compared to NH when both motions are generating similar values of $C_{L,avg}$.

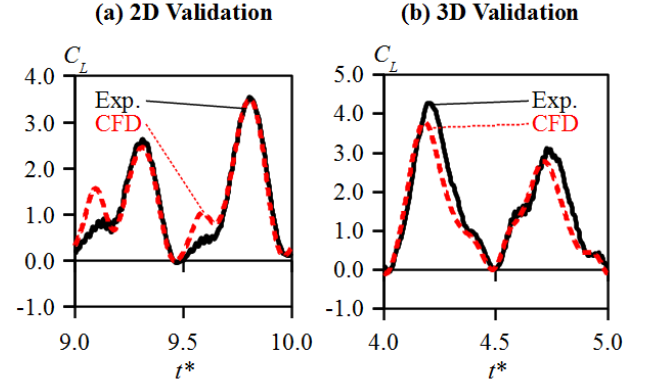


Figure 2. Validation for the (a) 2D and (b) 3D simulations by comparing C_L obtained from CFD (broken lines) with experimental measurements (solid lines) from [4, 5].

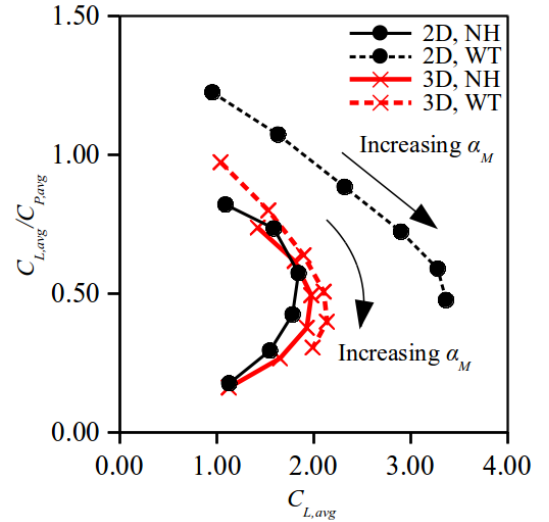


Figure 3. Aerodynamic performance of NH and WT motions in 2D and 3D as depicted by the plot of $C_{L,avg}/C_{P,avg}$ against $C_{L,avg}$.

As to why such differences in aerodynamic performance exist, we investigate the transient C_L and C_P trends for 2D and 3D NH and WT motions at $\alpha_M=45^\circ$ (figure 4). For all four cases, at the start of each stroke ($t^*=4.00$ and 4.50), C_L is almost zero due to the wing being stationary. Thereafter, the wing accelerates (see equations (1) and (2)) and attains positive α (see equations (3) and (4)). Hence, C_L increases rapidly and peaks near the mid-stroke ($t^*=4.25$ and 4.75) where the maximum heaving or flapping velocity occurs. Note that the C_L peak occurs slightly after mid-stroke for NH but slightly before mid-stroke for WT. This can be attributed to rotational lift [1]; specifically, pitching-up motions generate positive rotational lift while pitching-down motions generate negative rotational lift. Hence, for NH (figure 1a), negative rotational lift is generated before mid-stroke and positive rotational lift is generated after mid-stroke. This pattern of rotational lift shifts the C_L peak to a point slightly after mid-stroke.

The reverse is true for WT due to the wing generating positive rotational lift before mid-stroke and negative rotational lift after mid-stroke, and the C_L peak is shifted to a point slightly before mid-stroke.

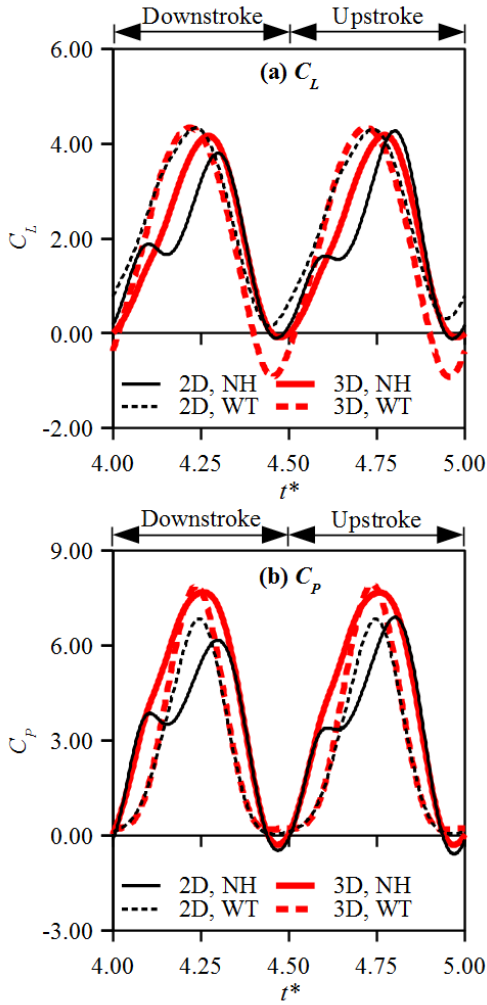


Figure 4. Transient (a) C_L and (b) C_p from the fifth flapping cycle of 2D and 3D NH and WT motions at $\alpha_M=45^\circ$.

In figure 4a, the 2D NH case features a decrease in C_L from $t^*=4.10$ to 4.20 and from $t^*=4.60$ to 4.70. This C_L decrease is not present for 2D WT nor the 3D cases. To explain this decrease, we refer to the vortex structures shown in figure 5, which depicts the contours of normalised vorticity at $t^*=4.20$ from the $\alpha_M=45^\circ$ cases. Here, vorticity is normalised by U_{ref} and c , hence $\omega^* = \omega / (U_{ref}/c)$, where ω and ω^* refer to vorticity and normalised vorticity, respectively. It is apparent from figure 5 that, for 2D NH, the D5_LEV has shed a considerable distance from the wing at $t^*=4.20$. This LEV shedding reduces the lift and drag forces over the wing, leading to a decrease in C_L and C_p for 2D NH from $t^*=4.10$ to 4.20 as shown in figure 4. Conversely, for 2D WT, the D5_LEV remains attached to the wing at $t^*=4.20$ (figure 5). Consequently, the LEV over 2D WT generates significantly higher aerodynamic forces than NH from $t^*=4.10$ to 4.30, resulting in higher C_L and C_p as depicted in figure 4. For the 3D cases, the difference in vortex structures is less apparent, and both NH and WT show a stably attached D5_LEV at $t^*=4.20$ (figure 5). This is likely due to the 3D effects (e.g. spanwise flow) that result in the formation of a stable LEV in the 3D cases (see [8, 9, 11, 13]).

Near the end of the stroke ($t^*=4.45$ and 4.95), 2D and 3D wings undergoing NH report near zero values of C_L (figure 4a). However, 2D WT shows a slightly positive C_L while 3D WT shows a

negative C_L peak near $t^*=4.45$ and 4.95 (figure 4a). This can be explained by referring to the normalised vorticity contours at $t^*=4.45$ (figure 6). For both 2D and 3D wings undergoing NH, the wing is nearly vertical at $t^*=4.45$ and the residual D5_LEV is behind the wing, thereby having little effect on C_L . As a result, for NH, C_L is close to zero at $t^*=4.45$ (see figure 4a). Conversely, for the 2D and 3D wings undergoing WT, the residual D5_LEV is above the wing at $t^*=4.45$. For 2D WT, D5_LEV covers the entire top surface of the wing while for 3D WT, D5_LEV covers only about half of the wing chord (figure 6). Accordingly, there may be a component of induced velocity generated by the vortex that acts downwards onto the wing's upper surface (figure 6) which causes the generation of negative C_L near $t^*=4.45$ and 4.95 as seen in figure 4a.

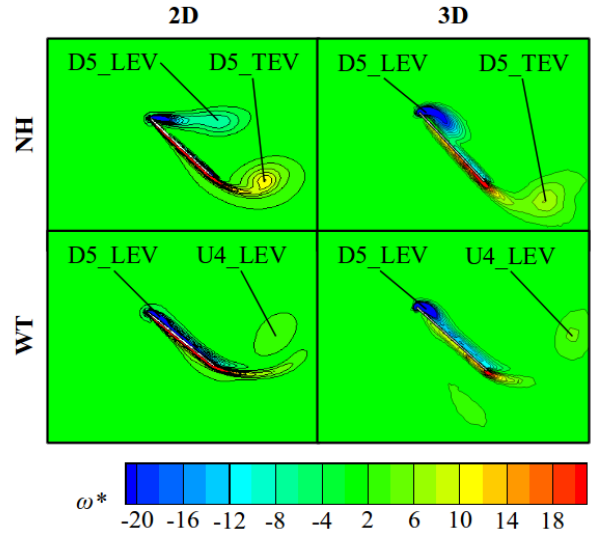


Figure 5. Contours of normalised vorticity for the $\alpha_M=45^\circ$ cases at $t^*=4.20$. For the 3D cases, the contours are taken from the plane coinciding with the R_2 position of the wing. “LEV” and “TEV” refer to the leading-edge vortex and trailing-edge vortex, respectively. The prefixes “U4” and “D5” refer to vortices that originate from the fourth upstroke and fifth downstroke, respectively.

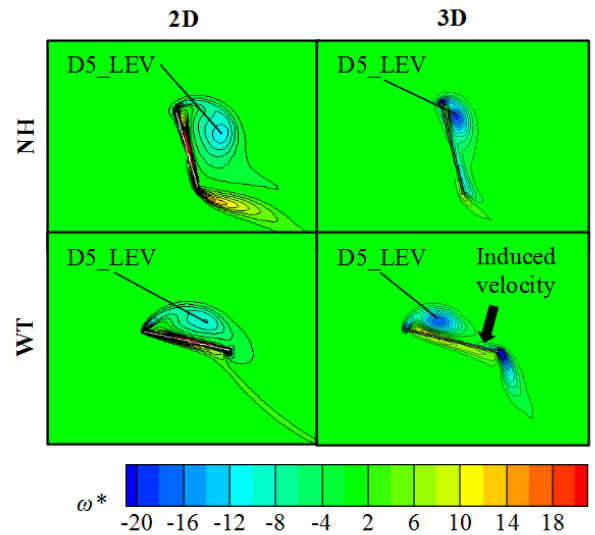


Figure 6. Contours of normalised vorticity for the $\alpha_M=45^\circ$ cases at $t^*=4.45$. For the 3D cases, the contours are taken from the plane coinciding with the R_2 position of the wing.

Contours of normalised pressure are plotted for the 2D and 3D wings undergoing WT at $\alpha_M=45^\circ$ (figure 7), where gauge pressure

(p) has been normalised by the reference dynamic pressure ($q=0.5\rho U_{ref}^2$). It is apparent from figure 7 that the induced velocity (see figure 6) creates a positive pressure region above the 3D wing undergoing WT, which generates negative C_L near $t^*=4.45$ and 4.95 (figure 4a). In contrast, the 2D wing has a low pressure region throughout the top surface due to the extent of the residual LEV. In other words, the 2D WT case shows a more favourable interaction between the wing and the residual LEV near $t^*=4.45$ and 4.95, which results in improved C_L generation.

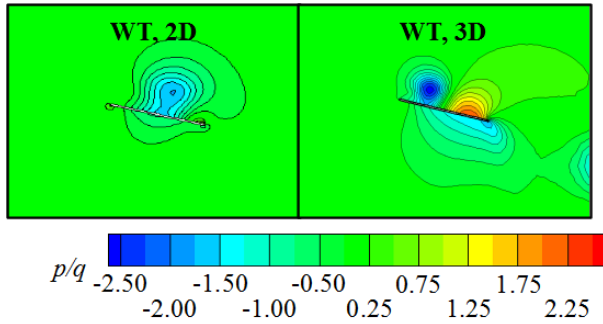


Figure 7. Contours of normalised pressure taken at $t^*=4.45$ for the 2D and 3D WT cases. For the 3D case, the contours are taken from the plane coinciding with the R_z position of the wing.

In terms of C_P , figure 4b shows that, for both 2D and 3D cases, NH incurs noticeably higher C_P near the beginning and the end of stroke compared to WT. This can be attributed to the fact that NH tends to have higher α at the start and the end of each stroke (see figures 1a and 1b), which generates higher aerodynamic drag that results in higher aerodynamic power. For the 2D cases, WT incurs higher C_P at mid-stroke (near $t^*=4.25$) compared to NH (figure 4b). This is likely due to the more stable LEV that remains attached to the wing in the case of WT as discussed earlier based on figure 5. The attached LEV gives rise to higher drag force which results in higher C_P for 2D WT near $t^*=4.25$.

Overall, the performance enhancement achieved by WT can be attributed to the following factors. In 2D cases, the initial pitching-down motion of NH induces LEV shedding while the initial pitching-up motion of WT delays LEV shedding. As a result, WT generates significant higher $C_{L,avg}$. In 3D, the LEV remains stably attached to the wing for both NH and WT. Hence, 3D WT does not achieve a significant increase in $C_{L,avg}$ that is seen in the 2D cases. In terms of $C_{P,avg}$, WT has comparatively lower $C_{P,avg}$ compared to NH due to WT starting and ending each stroke with low α , which results in low aerodynamic drag at the start and end of each stroke.

Conclusions

Numerical simulations have been conducted on 2D and 3D wings undergoing normal hovering (NH) and water treading (WT) motions. In 2D, WT yields significantly higher mean lift coefficient compared to NH. This can be attributed to the initial pitching-up motion of WT that delays the leading-edge vortex (LEV) shedding phenomenon. In contrast, during the initial pitching-down motion of NH, the LEV tends to detach from the wing surface. In 3D, both NH and WT feature stable LEVs and the lift enhancement achieved by WT is not significant. Additionally, the interaction between the wing and the residual LEV at the end of the stroke is beneficial in 2D WT, while the residual LEV from 3D WT induces a downward velocity component that results in the generation of negative lift near the end of the stroke.

In both 2D and 3D, WT incurs significantly lower aerodynamic power compared to NH. This is because WT begins and ends each flapping stroke at close to zero angle of attack (α). As a result, WT avoids the high α phase that NH encounters at the start and the end

of each stroke, which generates high aerodynamic drag with no apparent benefits. Consequently, WT incurs lower aerodynamic power and has significantly higher hovering efficiency. For the nominal parameter of 45° mid-stroke angle of attack, water treading outperforms normal hovering in terms of hovering efficiency by up to 54% in 2D and 29% in 3D. Hence, from a purely aerodynamic perspective, the water treading motion can be a promising alternative as the wing kinematics for FWMAV.

References

- [1] Dickinson, M.H., Lehmann, F.-O. & Sane, S.P., Wing Rotation and the Aerodynamic Basis of Insect Flight, *Science*, **284**, 1999, 1954–1960.
- [2] Ellington, C.P., The Aerodynamics of Flapping Animal Flight, *Amer Zool*, **24**, 1984, 95–105.
- [3] Freymuth, P., Thrust Generation by an Airfoil in Hover Modes, *Exp Fluids*, **9**, 1990, 17–24.
- [4] Lee, Y.J., Lua, K.B., Lim, T.T. & Yeo K.S., A Quasi-Steady Aerodynamic Model for Flapping Flight with Improved Adaptability, *Bioinsp Biomim*, **11**, 2016, 036005.
- [5] Lu, H., Lua, K.B., Lim, T.T. & Yeo, K.S., Ground Effect on the Aerodynamics of a Two-Dimensional Oscillating Airfoil, *Exp Fluids*, **55**, 2014, 1787.
- [6] Lua, K.B., Lim, T.T. & Yeo, K.S., Scaling of Aerodynamic Forces of Three-Dimensional Flapping Wings, *AIAA J*, **52**, 2014, 1095–1101.
- [7] Lua, K.B., Lee, Y.J., Lim T.T. & Yeo K.S., Aerodynamic Effects of Elevating Motion on Hovering Rigid Hawkmothlike Wings, *AIAA J*, **54**, 2016, 2247–2264.
- [8] Maxworthy, T., Experiments on the Weis-Fogh Mechanism of Lift Generation by Insects in Hovering Flight. Part 1. Dynamics of the ‘Fling’, *J Fluid Mech*, **93**, 1979, 47–63.
- [9] Maxworthy, T., The Fluid Dynamics of Insect Flight, *Ann Rev Fluid Mech*, **13**, 1981, 329–350.
- [10] Nagai, H. & Isogai, K., Effects of Flapping Wing Kinematics on Hovering and Forward Flight Aerodynamics, *AIAA J*, **49** 2011, 1750–1762.
- [11] Sane, S.P., The Aerodynamics of Insect Flight, *J Exp Biol*, **206**, 2003, 4191–4208.
- [12] Shyy, W., Lian, Y., Tang, J., Viieru, D. & Liu, H., *Aerodynamics of Low Reynolds Number Flyers*, Cambridge University Press, 2007.
- [13] Shyy, W., Aono, H., Chimakurthi, S.K., Trizila, P., Kang, C.-K., Cesnik, C.E.S. & Liu, H., Recent Progress in Flapping Wing Aerodynamics and Aeroelasticity, *Prog Aerosp Sci*, **46**, 2010, 284–327.
- [14] Tang, J., Viieru, D. & Shyy, W., Effects of Reynolds Number and Flapping Kinematics on Hovering Aerodynamics, *AIAA J*, **46**, 2008, 967–976.
- [15] Wang, Z.J., The Role of Drag in Insect Hovering, *J Exp Biol*, **207**, 2004, 4147–4155.
- [16] Weis-Fogh, T., Quick Estimates of Flight Fitness in Hovering Animals, Including Novel Mechanisms for Lift Production, *J Exp Biol*, **59**, 1973, 169–230.
- [17] Zheng, L., Hedrick, T. & Mittal, R., A Comparative Study of the Hovering Efficiency of Flapping and Revolving Wings, *Bioinsp Biomim*, **8**, 2013, 036001.